ELSEVIER

Mechanics of Materials 33 (2001) 403–421

MECHANICS OF MATERIALS

www.elsevier.com/locate/mechmat

Dynamic fracture of compositionally graded materials with cracks along the elastic gradient: experiments and analysis

C.-E. Rousseau, H.V. Tippur *

Department of Mechanical Engineering, Auburn University, 201 Ross Hall, Auburn, AL 36849-5341, USA

Received 24 April 2001

Abstract

Crack tip deformation and fracture parameter histories in compositionally graded glass-filled epoxy are evaluated for low velocity impact loading. The situations when the elastic gradient is unidirectional with crack orientation along the gradient are examined. The fracture behavior of graded compositions is studied relative to homogeneous counterparts made of identical constituents. Optical method of CGS and high-speed photography are used to measure crack tip deformations prior to crack initiation and during dynamic crack growth. The apparent stress intensity factors prior to crack initiation are determined using dynamic equivalent of the stationary fields for FGMs while crack tip fields for steadily growing cracks in FGMs are used for post-initiation situations. Results from finite element simulations up to crack initiation are in excellent agreement with the experimental evaluations. Post crack initiation stress intensity factor histories and crack growth resistance behaviors for FGMs with monotonically increasing and decreasing elastic gradient are strikingly different. When the crack growth occurs into material with progressively increasing filler volume fraction, continuously increasing $K_{ID}(t)$ is seen while a decreasing trend is observed when the gradient is of the opposite sense. The fracture behaviors are explained by independent fracture tests and fractured surface micrographs.

Keywords: Functionally graded material; Crack tip fields; Optical interferometry; Finite element analysis; Dynamic fracture

1. Introduction

The concept of using functionally graded materials (FGMs) arose in the mid-1980's as a way of improving the thermo-mechanical performance of spaceplane structures. Because of high thermal gradients, metallic structures have traditionally been coated with heat-resistant materials. However, thermal cycling and shock often results in cracking and spallation of the coating. Material gradation offers a way of maintaining the high strength of an inner core and the high thermal resistance of an outer layer while eliminating the deleterious effects of sharp interface. The performance of FGMs under dynamic loading conditions, primarily their fracture behavior is of interest to the present study.

Interest in the mechanics of FGM predates the coining of the term itself. Delale and Erdogan (1983) studied the crack tip field of a nonhomogeneous material with exponential Young's modulus variation in the direction of the crack and determined that the stress field at the crack tip retains the inverse square root singularity present

* Corresponding author. Fax: +1-334-844-3307.
E-mail address: htippur@eng.auburn.edu (H.V. Tippur).

0167-6636/01/$ - see front matter
PII: S0167-6636(01)00065-5

in homogeneous materials. Further works by Eischen (1987) and Jin and Noda (1994) reaffirmed that conclusion. Additionally, they asserted that the dominant terms in the crack tip stress field of an FGM are identical to those of a homogeneous material having the material properties of the FGM crack tip vicinity. Dynamic stress intensity factors for a mode-III crack lying in an elastic media with spatially varying elastic properties normal to crack surfaces has been studied analytically by Babaei and Lukasiewicz (1998). They have found SIF to vary with crack length to layer thickness ratio. Dynamic crack propagation in functionally graded particle dispersed material is numerically studied by Nakagaki et al. (1998) for shock loading to determine the effect of grading on crack severity as it propagates in the FGM. Chiu and Erdogan (1999) have examined one-dimensional wave propagation in FGMs having gradation in the direction of the incident pulse and observed considerable wave distortions as a rectangular pressure pulse propagates in the material. Expressions for the first stress invariant near steadily propagating dynamic cracks in a planar nonhomogeneous elastic medium has been made available by Parameswaran and Shukla (1999). The existence of the standard inverse $\sqrt{r}$ singularity associated with the dominant term has been demonstrated and nonhomogeneity specific higher order terms are reported.

To date very few fracture experiments involving FGMs, particularly on dynamic fracture, are reported. Dynamic crack growth in *discretely* layered polyester (modified with plasticizer) having graded elastic properties has been photoelastically studied by Parameswaran and Shukla (1998). They have shown that increasing toughness in the direction of crack growth reduces crack jump distance. Marur and Tippur (2000a) have studied the dynamic response of cracks situated at a graded *interface normal to the elastic gradient* and subjected to low velocity impact in three-point bending configuration. They have used a pair of optimally located strain gages and the assumption of locally homogeneous crack tip properties to evaluate dynamic mixed-mode stress intensity factor histories up to crack initiation. Using tup and anvil force histories as boundary conditions in an independent finite element analysis (FEA), dynamic stress intensity factors up to crack initiation were computed and shown to have excellent agreement with experiments.

In this paper, full-field optical measurements are used to examine the response of compositionally graded materials, with cracks oriented *along the direction of the gradient*, to dynamic impact. Although, the material used is microscopically heterogeneous, for the measurement scales used in this study it is treated as nonhomogeneous, isotropic continuum. Section 2 presents a brief theoretical background on the relevant displacement fields around growing cracks in FGMs. Section 3 details the material processing and material properties of the specimens used in this study. This is followed by a description of the experimental setup in Section 4. Optical measurements and the method of extracting fracture parameters are described in Section 5. Section 6 describes companion elasto-dynamic finite element simulations of the experiments. Finally, the results are presented and discussed in Section 7.

2. Crack tip fields in functionally graded materials

2.1. Stationary crack

Consider a semi-infinite crack oriented along the direction of the elastic gradient in an infinite nonhomogeneous, isotropic planar body. Using asymptotic analysis, Eischen (1987) has shown that the crack tip stress field in an FGM for a mode-I crack is of the form

$$\sigma_x + \sigma_y = \left(C_0 r^{-1/2} f_0^{\mathrm{I}}(\theta) + C_1 r^0 f_1^{\mathrm{I}}(\theta)\right) + \mathrm{O}\left(r^{1/2}\right), \tag{1}$$

where (r,θ) denote crack tip polar coordinates, f_0^{I}, f_1^{I} are angular functions, and C_0 and C_1 are the coefficients of the expansion with $C_0 = K_{\mathrm{I}}/\sqrt{2\pi}$ K_{I} being the mode-I stress intensity factor. Further, the angular functions have been shown to be identical to the ones for a crack in a homogeneous body. Accordingly, stress field description is identical to the homogeneous counterpart for the first two terms of the expansion. Moreover,

Rousseau and Tippur (2000) have determined experimentally that addition of an expression of the form $C_2 r^{1/2} f_2^{\mathrm{I}}(\theta)$ can be used adequately as a third term in the asymptotic expansion, where C_2 is an unknown coefficient, and f_2^{I} is defined as the same angular function used for homogeneous materials. Expressions for FGM in-plane displacement fields were also developed by Eischen (1987). It was found that asymptotic displacement terms proportional to $r^{1/2}$, r^0, and r^1 are identical to those of homogeneous materials, thus are independent of gradient. Terms of higher order are affected by gradient characteristics. Since the experimental methods used in this study measure surface slope, evaluation of expressions for out-of-plane displacement, w, is in order. Knowing the expression for $(\sigma_x + \sigma_y)$ and assuming plane stress conditions and constant thickness-wise strain $\varepsilon_z \approx 2w/B = -v(\sigma_x + \sigma_y)/E_0$, out-of-plane displacement can be obtained as

$$w \approx \frac{-vB}{2}\big(A_0 r^{-1/2} f_0^{\mathrm{I}}(\theta) + A_1 r^0 f_1^{\mathrm{I}}(\theta) + A_2 r^{1/2} f_2^{\mathrm{I}}(\theta)\big) + \mathrm{O}(r) \tag{2}$$

with $A_j = C_j/E_0$, where the subscript E_0 denotes the local value of crack tip Young's modulus. In the above, Poisson's ratio v is assumed to be constant in the FGM. One could potentially extend Eq. (2) for the case of a dynamically loaded stationary crack with the assumption that the inertial effects enter the coefficients in Eq. (2) $(A_i \equiv A_i(t))$ and the form of the equations remains unaltered.

2.2. Steady state dynamic crack growth

Consider a dynamically propagating crack along the direction of the gradient in a planar FGM. Let the crack be growing at constant velocity c in the X-direction. For a linear variation in shear modulus and constant material density on the one hand, and exponential variation in both elastic modulus and density on the other hand, using asymptotic analysis, Parameswaran and Shukla (1999) have developed equations describing crack tip stress fields. Explicitly, in the latter case, $\mu = \mu_{\mathrm{o}} \exp(\alpha X)$ and $\rho = \rho_{\mathrm{o}} \exp(\alpha X)$, where μ and ρ denote shear modulus and material density, the subscript o designates the original crack tip location (origin of the X and Y axes), and nonhomogeneity parameter α is a positive or negative constant. For steady-state conditions, location of the moving crack tip at any instant in time is defined at the origin of the x–y axes. As before, knowing the expression for $(\sigma_x + \sigma_y)$ from Parameswaran and Shukla (1999), and assuming plane stress conditions and constant thickness-wise strain, instantaneous out-of-plane displacement can be expressed as

$$w(t) = \frac{-vB}{2(1+v)(1-2v)}\left\{A_0(t) r_l^{-1/2} \cos\frac{\theta_l}{2} + A_1(t) + A_2(t) r_l^{1/2} \cos\frac{\theta_l}{2} - \frac{\alpha}{4\alpha_l^2} A_0(t) r_l^{-1/2} \cos\frac{3\theta_l}{2} + \frac{2\alpha\alpha_s}{(k+2)\left(\alpha_l^2 - \alpha_s^2\right)} B_0(t) r_s^{1/2} \cos\frac{\theta_s}{2}\right\}, \tag{3}$$

where

$$k = \frac{\lambda_0}{\mu_0}, \quad \alpha_l = \sqrt{1 - \frac{\rho_{\mathrm{o}} c^2}{\mu_0 (k+2)}}, \quad \alpha_s = \sqrt{1 - \frac{\rho_{\mathrm{o}} c^2}{\mu_0}},$$

$$r_l = \sqrt{x^2 + \alpha_l^2 y^2}, \quad \theta_l = \tan^{-1}\frac{\alpha_l y}{x},$$

$$r_s = \sqrt{x^2 + \alpha_s^2 y^2}, \quad \theta_s = \tan^{-1}\frac{\alpha_s y}{x},$$

$$A_0 = \frac{\left(1+\alpha_s^2\right)\left(1-\alpha_l^2\right)}{4\alpha_s\alpha_l - \left(1+\alpha_s^2\right)^2} \frac{K_{\mathrm{ID}}}{\mu_c\sqrt{2\pi}},$$

$$B_0 = \frac{2\alpha_l}{1+\alpha_s^2} \frac{1-\alpha_s^2}{1-\alpha_l^2} A_0.$$

In the above, λ is Lamé's constant, and $\mu_{\mathrm{c}} = \mu_{\mathrm{o}} \exp(\alpha c t)$. Coefficients A_0, A_1 and A_2 are unknown coefficients of the asymptotic expression. Evidently, as the material gradient parameter α becomes zero, the equations reduce to that of its homogeneous counterpart (Freund and Clifton, 1974).

In the limit $c \to 0$, Eq. (3) should yield results for the case of a dynamically loaded stationary crack with inertial effects entering the coefficients

A_0, A_1, and A_2. The limit analysis, however, shows that the form of the expression for $w(t)$ is unlike the quasi-static counterpart (Eq. (2)). That is, crack velocity dependent multiplier in the fourth term approaches a finite value while fifth term seems to become unbounded as c approaches zero. Such a behavior is attributed to the fact that the dilatational and rotational terms in the equations of motion remain coupled and become uncoupled only when the nonhomogeneity parameter α becomes zero. It is believed (Parameswaran and Shukla, 2000) that the coupling weakens at low velocity causing the fifth term of the equation to drop out.

3. Material processing and elastic characterization

The specimens tested in this study were prepared from an epoxy system combined in varying quantities with solid soda-lime glass spheres (mean diameter 42 μm). The slow curing and low shrinkage characteristics of the epoxy insured minimal residual stresses in the particulate composite. Microscopic examination of the composite showed uniform dispersion of the inclusions within the matrix in all directions.

Prior to casting the FGMs specimens, homogeneous (i.e., constant volume fraction, V_f) samples were prepared by first combining the two-part epoxy mixture, then including and mixing the glass particles up to the specified volume fraction. The resulting mixture was then poured into a mold and allowed to cure and solidify prior to removal and machining.

Elastic properties of each of these homogeneous samples were determined by indirect means of ultrasonic pulse-echo measurement, using 10 MHz longitudinal and 5 MHz shear transducers. Longitudinal (C_l) and shear wave (C_s) speeds in a plate are related to the elastic constants and density as

$$C_l^2 = \frac{E}{\rho(1-\nu^2)}, \quad C_s^2 = \frac{\mu}{\rho}.$$

After measuring the density of the homogeneous samples and their wave speeds, dynamic Young's moduli and Poisson's ratios were determined from the above equations. Fig. 1(a) shows variation of wave speeds and density with volume fraction of filler in the matrix. Following are plots of elastic modulus and Poisson's ratio shown in Fig. 1(b). Except for Poisson's ratio which decreases, other properties are observed to increase monotonically with V_f. A nearly three fold increase in Young's modulus is seen when V_f is varied between 0 and 0.5. For the same volume fractions, Poisson's ratio decreases from 0.37 to 0.32.

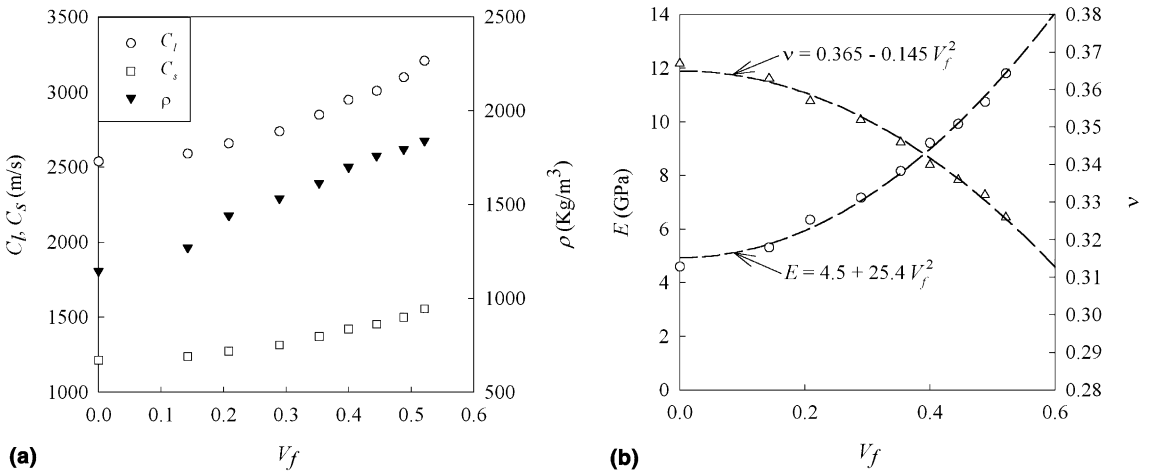

Fig. 1. Dynamic properties of glass-filled epoxy with different volume fraction of the filler: (a) wave velocities and density; (b) Young's modulus and Poisson's ratio.

FGM samples were made as described by Butcher et al. (1999), by allowing glass beads to sink to the bottom of a vertical mold, prior to solidification of the composite. In the present work the casting parameters were such that the resulting compositional gradient extended over a height of 37 mm, and was saddled by regions made of unfilled epoxy and of epoxy with nearly 50% filler volume fraction. Fig. 2(a) shows unidirectional asymmetric sigmoidal variations of (E/ρ) and v for a typical FGM casting. (Note that both E and ρ also follow increasing asymmetric sigmoidal gradient variations (not shown).) The compositional gradient of matrix and filler distributions provide ratios in dynamic Young's modulus of stiff and compliant sides of the FGM $(E_{\text{stiff}}/E_{\text{compliant}})$ of 2.5, and ratio $((E/\rho)_{\text{stiff}}/(E/\rho)_{\text{compliant}})$ of 1.5. The castings were machined to get FGM samples with properties shown in the un-shaded region of Fig. 2(a). Geometry and loading configuration of a FGM beam sample machined from the cast plates is shown in Fig. 2(b).

Three types of specimens of identical geometry (152.3 mm × 37 mm × 6 mm) and loading configuration (Fig. 2(b)) were examined, the first being a cracked homogeneous beam, and the others being FGMs having cracks either on the compliant or the stiff side of the sample. Throughout this paper E_2 will be used to designate the value of Young's modulus at the impact location (edge opposite the crack tip), and E_1, the modulus at the bottom edge of the sample (behind the crack tip). Therefore, *a ratio $E_2/E_1 > 1$ corresponds to the case of a sample with a crack on the compliant side, being impacted on the stiff side. A ratio $E_2/E_1 < 1$ designates an FGM sample with a crack on the stiff side being impacted on the compliant side. For a homogeneous (constant volume fraction) sample E_2/E_1 ratio is* 1. All specimen surfaces were machined flat to fulfill the stringent requirements associated with optical measurements. Surfaces to be examined were coated with thin aluminum film (a few angstroms thick) transferred from an optical flat by means of a very thin layer of epoxy (same as matrix material). An edge crack was introduced into the samples with a high-speed diamond saw. Subsequent optical examination did not reveal any crack tip residual stress effects.

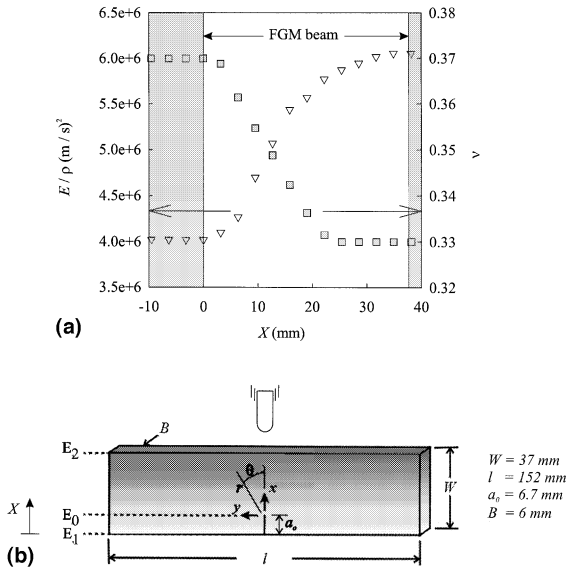

Fig. 2. Material description: (a) material property variation along FGM casting (material properties after machining of FGM samples are shown un-shaded); (b) sample dimension and loading configuration.

4. Optical method and experimental set-up

The optical method of reflection coherent gradient sensing (CGS) (Tippur et al., 1991) was used to measure surface slopes along the crack orientation prior to, and following crack initiation. A schematic of the optical set-up is shown in Fig. 3. An argon-ion laser beam (wave length 514 nm) is collimated and expanded to a diameter of 50 mm. Upon reaching the specimen, the beam is reflected, carrying information associated with the local out-of-plane deviations of the surface from its original state of flatness. A pair of Ronchi gratings diffracts this incident beam perpendicular to the grating lines, in effect shearing the image. Fringe patterns are generated at locations of light beam interference. These are carried in a linear array of spots to the back focal plane of a filtering lens, where either the +1 or −1 diffraction orders is filtered and imaged. The fringes represent surface slope contours in the x-direction (along the crack line and perpendicular to the grating lines), and are described by the governing equation of CGS

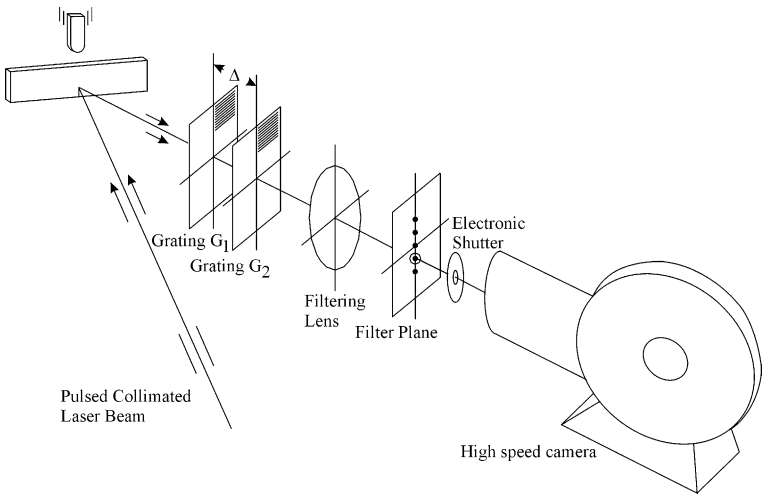

Fig. 3. Schematic of reflection CGS optical set-up used for mapping dynamic crack tip deformations.

$$\frac{\partial w}{\partial x} \approx \frac{\delta w}{\delta x} = \frac{Np}{2\Delta}, \quad N = 0, \pm 1, \pm 2, \ldots, \tag{4}$$

where N denotes fringe orders, p is the pitch of the gratings (25 μm), and Δ is the grating separation distance (49 mm) and $\delta(\cdot)$ is the difference operator. Assuming plane stress conditions, the out-of-plane displacement w is related to the in-plane normal stresses and elastic constants as

$$w \approx -\frac{vB}{2}\left(\frac{\sigma_x + \sigma_y}{E}\right),$$

where B is the undeformed thickness of the specimen. It should be pointed out that CGS being a surface slope measuring method, it is insensitive to uniform surface displacement (or, the so-called T-stress effect). Components of the experimental set-up are described next.

The experimental set-up comprises of an impactor, pulse-laser, CGS interferometer and a high-speed camera. During the experiment, a pneumatically operated impactor with a steel cylindrical head is launched towards the specimen. The air pressure (bottle pressure 80 psi) propels the hammer at a speed of ~5.3 m/s. During its descent, the hammer first triggers a photodetector which opens the iris of an electronic shutter located in front of the high-speed camera, allowing light to reach its internal cavity. The specimen is subjected to one point symmetric impact. A 0.03 mm thick adhesive-backed copper tape placed on the top edge of the beam closes an electric circuit when it is contacted by the hammer. This triggers a bank of pulse generators and in turn the laser to begin pulsing (for a total time of 368 μs) at a repetition rate of 5 μs (200,000 frames per second), with a pulse width of 50 ns. At the end of that period, the electronic shutter is closed, preventing stray light rays from entering the camera, thus avoiding re-writing on the film.

A Beckman and Whitley Model 339 Continuous Writing Sweeping Image Camera was used to capture the information emanating from the specimen surface. A 1.2 m long Kodak (T-Max 400 g/W) film is held stationary in the film track waiting to be swept by discrete images reflected from a turbine-driven three-facet mirror. The turbine, driven by compressed air (bottle pressure 100 psi, inlet pressure 45 psi), rotates at ~800 rps. With the settings used, 73 images can be written over a 270° angle.

5. Optical measurements

Several experiments in each category of FGM and homogeneous materials were carried out. For brevity, four select interferograms are shown for

each experiment, at times 25, 75 (near crack initiation), 100, and 125 μs after impact. CGS fringes for the homogeneous material are shown in the first column of Fig. 4. Fringes for the FGMs with crack located on compliant and stiff sides of the gradient are shown in the second and third columns of Fig. 4, respectively. The homogeneous beam has a volume fraction of 0.42, and an elastic modulus of 9.6 GPa. The FGM with crack on the compliant side ($E_2/E_1 \sim 2.9$) has elastic moduli approximately between 4 and 11 GPa with a value of $E_0 \sim 5.6$ GPa at the crack tip. Terminal values of Young's moduli are nearly the same for the FGM with crack on the stiff side ($E_2/E_1 \sim 0.45$), with crack tip $E_0 \sim 10$ GPa. Further details of the material properties of the tested specimens are presented in Table 1.

At the impact point of the homogeneous sample, instantaneous CGS fringes are expected to be similar to the ones predicted by the classical Flamant's solution (Johnson, 1998) for a line load acting on the edge of a semi-infinite planar body. The corresponding theoretical contours of $\partial w/\partial x$ are shown in Fig. 5(a) and compare favorably with those obtained from the experiments (Fig. 4, first column) at the impact point. Large frontal lobes (corresponding to positive surface slope; "positive fringes") flanked on both sides by lobes of nearly equal size (corresponding to negative surface slope; "negative fringes") are observed. Apogee of the positive and negative fringes are 90° apart. Impact point fringes for the FGM with crack on the compliant side ($E_2/E_1 > 1$) are very different. From the time of impact, the positive fringes are dwarfed when compared to the two enlarged negative fringes, until the latter are themselves overshadowed by the more prevalent singularity of the approaching crack. Loading point fringes for the FGM with crack on the stiff side ($E_2/E_1 < 1$) present yet a different pattern. First, note the comparatively more numerous fringes at the loading point, mainly due to the more compliant properties pertinent to that region. In addition, larger positive fringes are in contrast to the diminished size of the negative fringes. These qualitative differences in the deformation patterns are indicative of the influence of variation in the elastic characteristics as the interior of the material is approached from the impact location in the $-x$ direction while material characteristics remain unchanged in the y-direction at a given value of x. The crack tip deformations being central to the present research, these differences at the impact location will not be further pursued here.

Classical K-dominant crack tip solution for $\partial w/\partial x$ fringes in homogeneous materials are also shown in Fig. 5(a). Here the apogee of the positive and negative fringes is 120° apart. These again qualitatively resemble the experimental results obtained in the first column of Fig. 4. At the crack tip, one set of frontal (positive fringe) and two sets of equally prominent lateral fringe lobes (negative fringes) are present. Note also that remote from the two singular regions, the light intensity distribution in the far-field remains essentially uniform and unchanged, indicating no detectable deviation from the initial flatness. Conditions for the FGM with crack on the compliant side ($E_2/E_1 > 1$, Fig. 4) are notably different. Crack tip fringes appear to be constricted vertically throughout the entire sequence of events. A set of horizontal parallel fringes appears in the zone between the crack tip and impact point, and seems to be carried beyond the field of vision. In this case, the compressive stress waves progressively slow down as they encounter more compliant material when they propagate away from the stiff edge (see Fig. 5(b)). Under these conditions, the presence of this "soft support" remote from the loading point generates relatively larger disturbances in these regions in the form of parallel fringes. Crack tip fringes for the FGM with the crack on the stiff side ($E_2/E_1 < 1$, Fig. 4) of the gradient have a similar appearance to those of the homogeneous material. Here, the compressive stress waves generated at the compliant edge progressively encounter stiffer material and hence speed up during propagation away from the compliant edge. Well formed and nearly equisized front and rear fringe lobes are present. Additionally, a relatively uniform far-field is observed in this specimen.

For the homogeneous sample ($E_2/E_1 = 1$) with a volume fraction of 0.42 and a longitudinal velocity of ~2980 m/s, approximately 12.5 μs are required for the initial compressive waves to reach the bottom of the beam. The reflected tensile

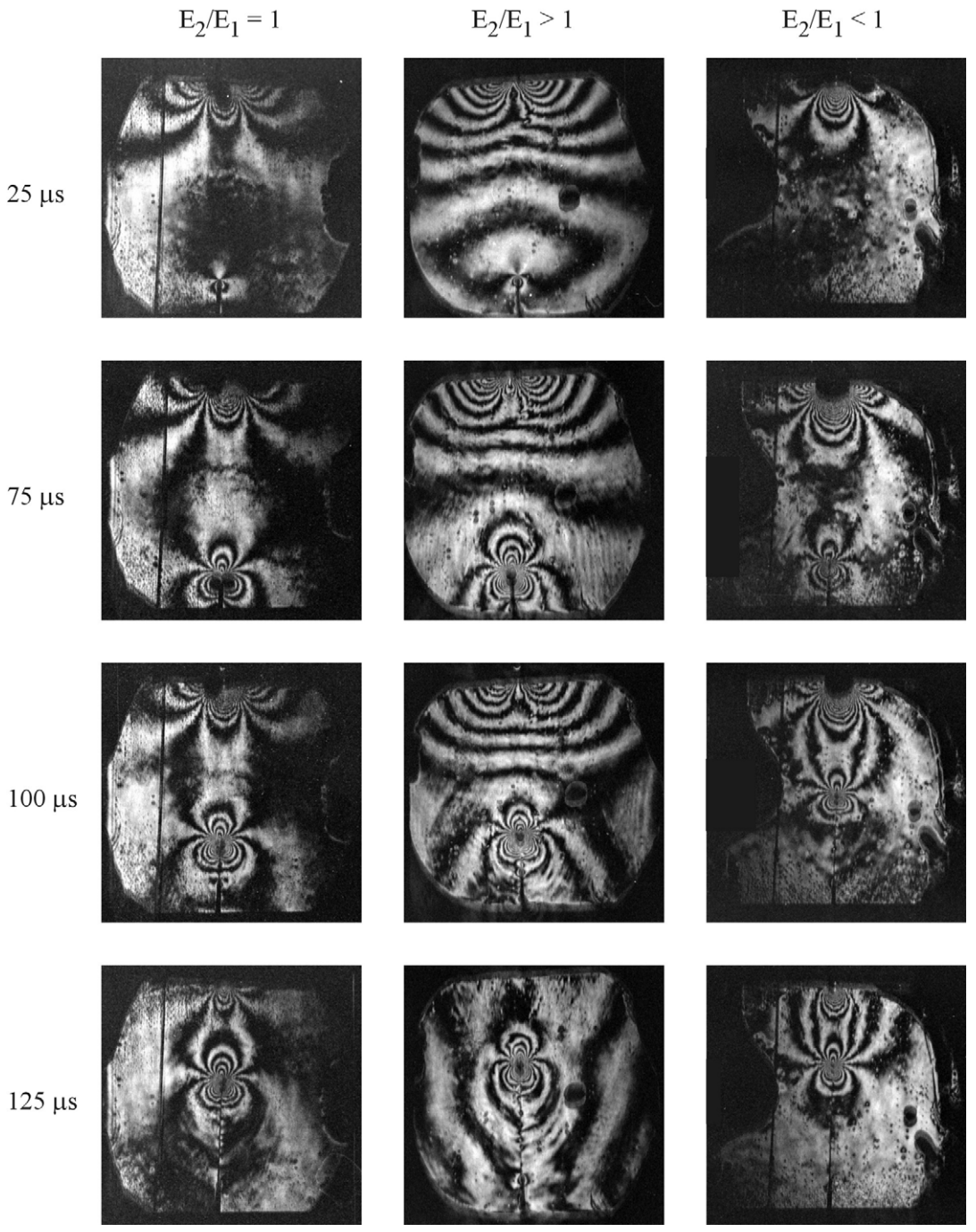

Fig. 4. Representative crack tip interference representing surface slope $\delta w/\delta x$ contours for homogeneous and FGM samples (fringe sensitivity 0.015°/fringe).

Table 1
Material properties at various locations along tested specimens

	Location	V_f	C_l (m/s)	E (MPa)	ν	ρ (kg/m^3)
FGM crack on compliant side $E_2/E_1 > 1$	Compliant edge	0.00	2488	3811	0.37	948
	Crack tip	0.16	2614	5595	0.36	1333
	Stiff edge	0.50	3155	11 130	0.33	1812
FGM crack on stiff side $E_2/E_1 < 1$	Stiff edge	0.49	3095	10 610	0.33	1788
	Crack tip	0.46	3050	10 210	0.33	1768
	Compliant edge	0.03	2550	4740	0.36	1175
Homogeneous $E_2/E_1 = 1$	–	0.42	2980	9600	0.34	1735

waves load the crack tip 15 μs after the impact. However, for this relatively stiff sample, this is not evident from the optical records (due to sensitivity limitation) and no significant fringe patterns are observed at the crack tip until about 25 μs. Following that, crack tip fringes progressively enlarge and become more numerous up to ~85 μs, when initiation takes place. After initiation, size and number of the fringes do not appear to be altered. Little disturbance in fringe shape is detected subsequently as the crack propagates through the material.

Average longitudinal wave speed

$$\left(\overline{C}_l = \frac{1}{W}\int_{-a}^{W-a} C_l(x)\,\mathrm{d}x\right)$$

for the FGM specimen with crack on the compliant side ($E_2/E_1 > 1$) is ~2910 m/s. Time for the arrival of the first compressive waves at the crack tip after impact is 10 μs, while first reflected tensile waves reach the crack tip at approximately 15 μs. Signs of loading and deformations do appear clearly at ~20 μs (not shown) in the form of crack tip fringes. It is important to remember here that compressive waves progressively slow down as the crack tip is approached while the reverse is true for the reflected tensile waves. The crack initiates approximately 85 μs after impact. The first few optical records following initiation show further increase in size of the fringes (all the frames are not shown in Fig. 4 for brevity) as the crack propagates, contrary to the homogeneous case discussed above. At 100 μs, however, the size of the fringes seems to remain constant but the fringes are subjected to significant distortion. The disturbances cannot be attributed solely to wave interference since the same is not perceived in the homogeneous case. One must conclude therefore that higher levels of energy are expended to maintain continued crack motion.

The FGM with the crack on the stiff side ($E_2/E_1 < 1$) experiences average longitudinal velocity of ~2900 m/s over the height of the beam. Again, this velocity corresponds to times of ~12.5 μs for a compressive wave to reach the bottom edge, and ~2.5 μs for a tensile wave to reflect to the crack tip. From the fringe patterns, the crack tip shows the first signs of loading at about 25 μs. In this case, the incoming compressive waves from the contact point travel progressively faster towards the crack tip while the reverse occurs for the reflected tensile waves. The size of the crack tip fringes increases gradually until initiation at about 90 μs. Interestingly, the size of these fringes does not increase as the crack propagates. As the crack moves into a softer material, higher deformation, consequently larger fringes would be expected. The dimensional constancy of these fringes may be an indication that smaller deformation, thereby lower fracture energy is required to cause the crack to continue its advance.

Finally, an observation pertinent to FGM and homogeneous specimens can be made from the previous discussion: compressive and tensile waves arrive at the original crack tips at approximately

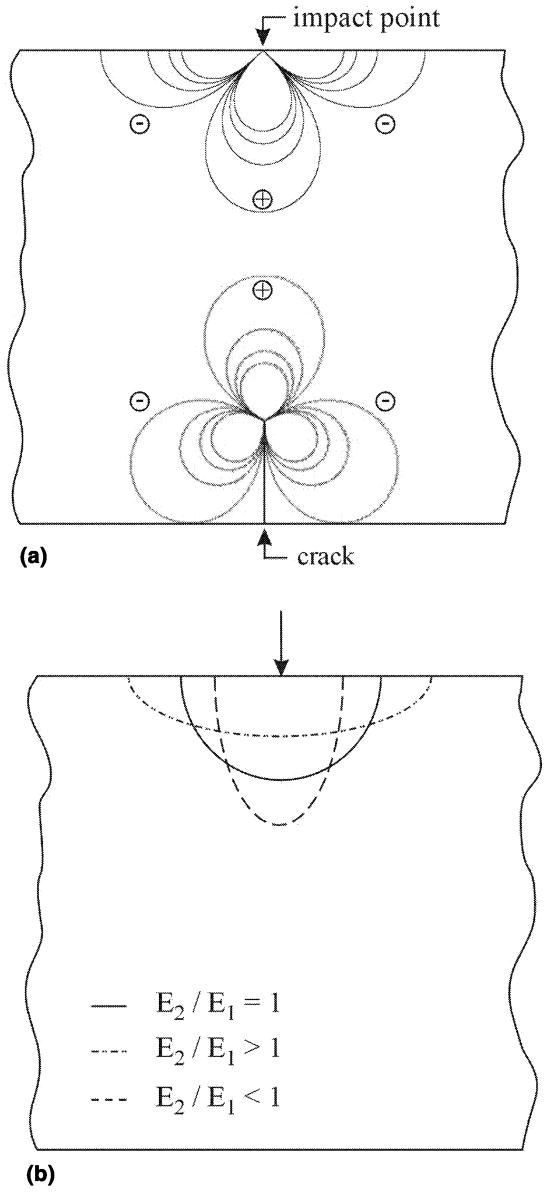

Fig. 5. Anticipated CGS contours at load point and at crack tip of a homogeneous sample (a). Schematic depicting instantaneous compressive stress wavefronts in FGM and homogeneous media (b).

the same times for all the specimens since the average longitudinal wave speeds are nearly same. Therefore, initially crack tip loading rates are nearly the same. Local state of the individual crack tips, as well as nonuniform wave reflections from the edges will contribute to varying conditions in crack initiation and propagation between the different specimens. This aspect will be pursued later.

5.1. Extraction of stress intensity factors from interferograms

Overdeterministic least-squares analysis of optical data (Tippur et al., 1991) was used to extract instantaneous stress intensity factors. Briefly, the method consisted of digitizing the interferograms around the crack tip to obtain fringe order N and location (r,θ) data. The previous studies (Tippur et al., 1991; Rousseau and Tippur, 2000) on crack tip fields using the method of CGS have indicated that in view of crack tip triaxiality in finite thickness samples, the data in the region $r/B > 0.4$ and $90° < |\theta| < 135°$ are most favorable for accurately determining the stress intensity factors in homogeneous and FGM samples under mode-I conditions. By minimizing the least-squares error $((\delta w/\delta x) - (Np/2\Delta))^2$ (w as given in the right-hand side of Eq. (2) or (3) at all digitized data points with respect to the unknown coefficients A_0 ($\propto K_{ID}$), A_1, A_2, and B_0) the stress intensity factor is evaluated. It should be pointed out that the analysis required value of the nonhomogeneity parameter α known a priori. Hence, Young's modulus and density data were first fitted with an exponential variation of the form $E(x) = E_0 \exp(\alpha X)$ to extract the scalar α in Eq. (3) (for example, see Fig. 6(a)). The constant α was determined such that experimental and analytical crack tip moduli would be the same, while maintaining approximately equal slopes in both curves *in the region where optical data was analyzed*. The value of α in case FGM with crack on the compliant size is 0.04 mm^{-1} and the one with crack on the stiff side is -0.015 mm^{-1}. The results shown in Fig. 6(b) will be discussed in Section 7.

6. Numerical simulations

Companion plane stress elasto-dynamic finite element simulation of all the three categories of experiments was performed. The simulations were limited to *dynamically loaded stationary crack* to

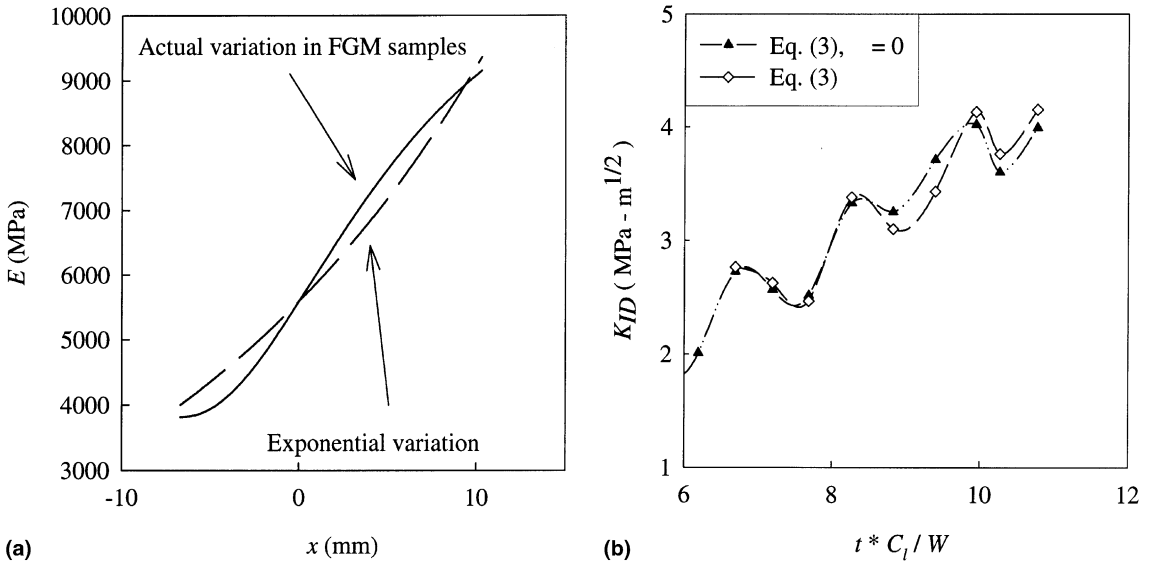

Fig. 6. Comparison between methods of evaluating apparent dynamic stress intensity factors in FGM with $E_2/E_1 > 1$: (a) determining nonhomogeneity α (0.04 mm^{-1}) for the FGM sample; (b) estimated SIF parameters from the fringes.

extract dynamic stress intensity factor history up to crack initiation (determined by the experiments). A two-dimensional quadrilateral mesh (not shown) of 8-noded isoparametric elements with two degrees of freedom per node was used in the analysis. Because of symmetry, only one-half of each sample is modeled, with approximately 10 000 nodes and 3300 elements. Singular elements were not defined at the crack tip. However, crack tip vicinity was highly refined for accurate evaluation of crack tip parameters. Simulations were conducted as a one point symmetric impact of an elastic planar medium by a rigid impactor, by imposing the downward velocity of the impactor (5.3 m/s) to the topmost node in the plane of the crack. No other boundary conditions were applied to the model. The Newmark time-integration scheme was used with a minimum time step of 0.04 μs.

Material property variations for FGMs were imposed using a technique developed by Rousseau and Tippur (2000). Briefly, the method consists of solving a steady-state heat transfer problem to achieve a specified temperature variation, and defining the necessary material properties to be functions of temperature with coefficient of linear expansion zero uniformly. Since the temperature distribution in the model follows material property variation of the actual specimens, finite element material properties do follow the behavior of their counterpart also. Gradients in dynamic Young's modulus and density were thus implemented. Poisson's ratio was kept constant at an average value of 0.34 in these computations.

In the immediate vicinity of the crack tip, Eqs. (2) and (3) for displacement may be truncated to the leading term and used for FGMs in the limit $r \to 0$. Thus, within a small region, FGM crack opening displacement is described as

$$\delta_y(t)|_{\theta=\pm\pi, r\to 0} = \frac{8\overline{K}_1^{\mathrm{d}}(t)}{E_0}\sqrt{\frac{r}{2\pi}}. \tag{5}$$

Here, ε_0 is the crack tip Young's modulus. The variation of $\overline{K}(r, \pm\pi)$ obtained from the finite element solution is plotted and its extrapolated value at the crack tip is

$$|K| = \lim_{r\to 0} |\overline{K}|. \tag{6}$$

This technique of extracting crack tip parameters in FGMs was used successfully by Marur and Tippur (2000b) in numerical computation of mixed-mode transient fracture parameters of

functionally graded interfaces subjected to low velocity impact loading, up to crack initiation.

7. Results and discussion

7.1. Crack initiation

Crack growth history was determined from fringe patterns, taking the crack tip to be the point of convergence of the outer three lobes (positive and negative fringe orders). For subsequent analyses, since the crack tip conditions (elastic properties and fracture toughness) are different in each sample, time is normalized with respect to the dilatational wave speed at the instantaneous crack tip location and the specimen height: $T = t \times C_l/W$ for comparison. Crack initiation occurred between T of 6.4–6.8 after impact for the homogeneous specimen. Evidence of crack motion is seen between T of 6.0–6.4 and 7.0–7.4 for the FGMs with $E_2/E_1 > 1$ and $E_2/E_1 < 1$, respectively. (Note that the values of T reflect the uncertainty involved in determining crack initiation from the high-speed images recorded with an inter-frame rate of 5 μs.) Accordingly, the behavior of the homogeneous material appears to fall in between those of the two FGMs. This observation is in agreement with independent numerical simulations (Rousseau, 2000) on FGMs and homogeneous samples with idealized linear elastic gradients having identical crack tip elastic properties.

To confirm that the above differences in crack initiation times are indeed predominantly due to elastic gradient, simulations of *uncracked* homogeneous and FGM beams of identical dimensions subjected to 5 m/s impact were carried out. Wave propagation through the material was monitored using instantaneous contour maps of $(\sigma_x + \sigma_y)$ in all three cases. Details of these simulations are found in Rousseau (2000) and only pertinent results are highlighted here. Elastic property E/ρ varied (between 4×10^6 and 6×10^6 m^2/s^2 – close to the ones in the optical studies) *linearly* between the top and bottom edges of FGM beam samples while the homogeneous counterpart had a uniform E/ρ value equal to the mean value of linear variation in FGMs. Poisson's ratio was equal to 0.33

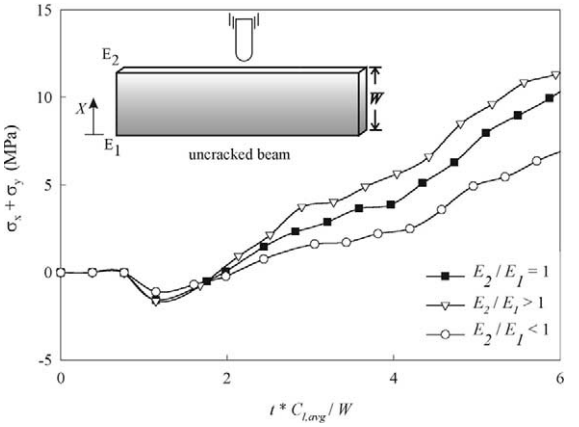

Fig. 7. $\sigma_x + \sigma_y$ at a location $(X = 0.2W,\ Y = 0)$ in uncracked beams, with linearly varying elastic moduli, subjected to one point impact by a rigid projectile.

in all cases. Thereby, average wave speeds in each case was the same and the influence of the elastic gradients was isolated. As tensile waves reflect from the bottom edge, they accelerate towards the crack tip for FGMs with $E_2/E_1 > 1$, decelerate for FGMs with $E_2/E_1 < 1$, and remain unaltered in the homogeneous case. The consequence of this is illustrated by the first stress invariant history in the uncracked beam at the location corresponding to that of the crack tips in experiments. In Fig. 7, the location of interest first experiences the effect of the downward traveling compressive waves, which are soon neutralized by the reflected tensile waves. The FGM with $E_2/E_1 > 1$ is consistently subject to higher tensile stresses than its counterparts. The homogeneous beam experiences slightly lower tensile stresses at any given moment in time, followed by the FGM with $E_2/E_1 < 1$. Consequently, crack initiation would be expected to occur in this order, as recorded in the experiments.

7.2. Crack extension

Crack extension with respect to time elapsed from crack initiation is plotted in Fig. 8(a). The behavior of all the beams is similar up to about $T_i = (t - t_i) \times C_l/W \sim 3.3$ (i.e., 35 μs after initiation) (t_i being time at crack initiation measured after impact) following the onset of growth. At that point, crack propagation of the FGM with

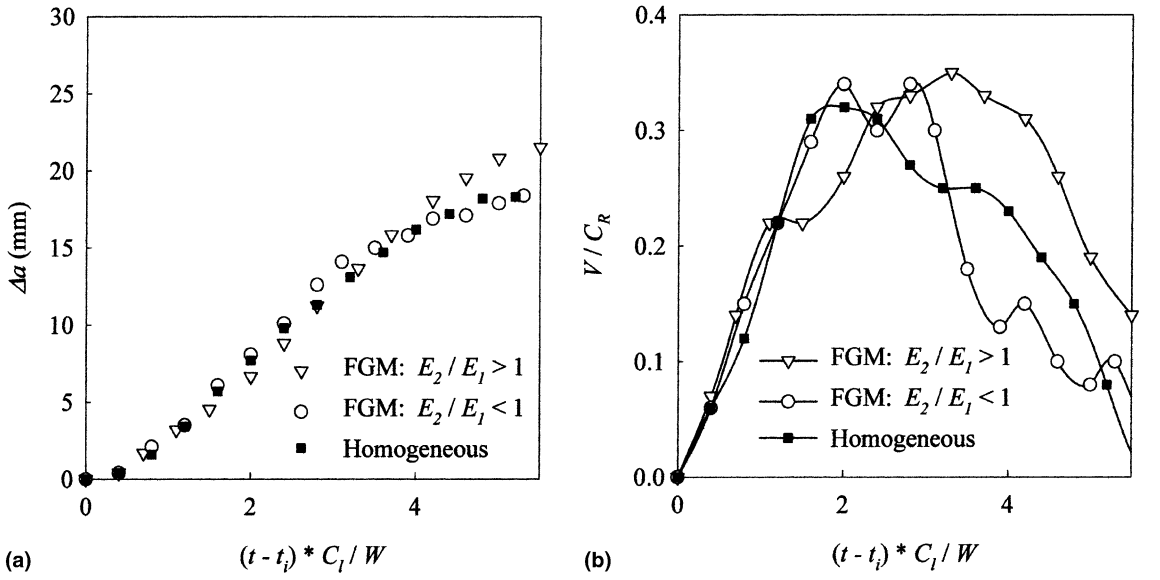

Fig. 8. Crack growth behavior: (a) crack extension; (b) crack velocity (t = time from impact; t_i = time at crack initiation).

ratio $E_2/E_1 > 1$ continues at the same rate whereas the homogeneous crack slows down. The FGM sample with a crack on the stiff side experiences growth similar to that of the homogeneous material.

The crack growth history is numerically differentiated using central difference scheme. The corresponding velocities (normalized relative to the *local* Rayleigh wave speed) are plotted in Fig. 8(b). Oscillations in velocity are expected due to the finite specimen size resulting in the arrival and interference of compressive and tensile waves that reflect from the horizontal and vertical edges, loading or unloading the crack tip at different times. Acceleration (initially $\sim 16 \times 10^6$ m/s^2 in all cases) reaches $\sim 28 \times 10^6$ m/s^2 in the homogeneous material, bringing its crack velocity to a maximum of $0.32C_R$ at $T \sim 2.0$. Acceleration for the FGM with crack on the compliant side reaches approximately $\sim 23 \times 10^6$ m/s^2 with the crack velocity attaining its peak of $0.35C_R$ later, at $T \sim 3.3$. At $T \sim 2.0$ after initiation, the FGM with crack on the stiff side experienced a much higher acceleration of $\sim 48 \times 10^6$ m/s^2, bringing the peak crack velocity to $0.34C_R$. (It must be noted, however, that these accelerations, being numerically determined second derivatives of crack growth data, should be viewed merely as estimates.) Peaks of the velocity curves are immediately followed by deceleration as the crack approaches the top edge of the beam. The FGM with $E_2/E_1 < 1$ shows relatively higher crack deceleration than the other two material. Interestingly, the deceleration of the homogeneous material is again sandwiched between those of the two FGMs.

7.3. Dynamic stress intensity factor

Stress intensity factors were first evaluated prior to and following crack initiation using Eqs. (2) and (3), respectively.

First, the degree of influence of the elastic nonhomogeneity specific terms in Eq. (3) on the stress intensity factors in the present investigation was determined. As an example, the results for the case of $E_2/E_1 > 1$ are shown in Fig. 6(b) as open symbols. (The necessary value of the nonhomogeneity parameter was obtained as described earlier in Section 5.) Also shown in the same plot are the extracted values (solid symbols) of K_{ID} obtained by setting the nonhomogeneity parameter α to zero thereby dropping the fourth and fifth terms

in the curly brackets of Eq. (3) from the analysis. This is equivalent to analyzing the experimental results using a *locally* homogeneous material assumption. The stress intensity factor results thus obtained using Eq. (3) have a ±5% difference between them. (If steeper property gradients were to exist, the FGM specific terms in Eq. (3) could potentially have higher contributions to the fracture parameters.)

Symbols in Fig. 9(a) represent optically extracted dynamic stress factor history for the *homogeneous* material ($V_f = 0.42$). Finite element results are also plotted as a solid line, up to the time of crack initiation, t_i (determined experi-

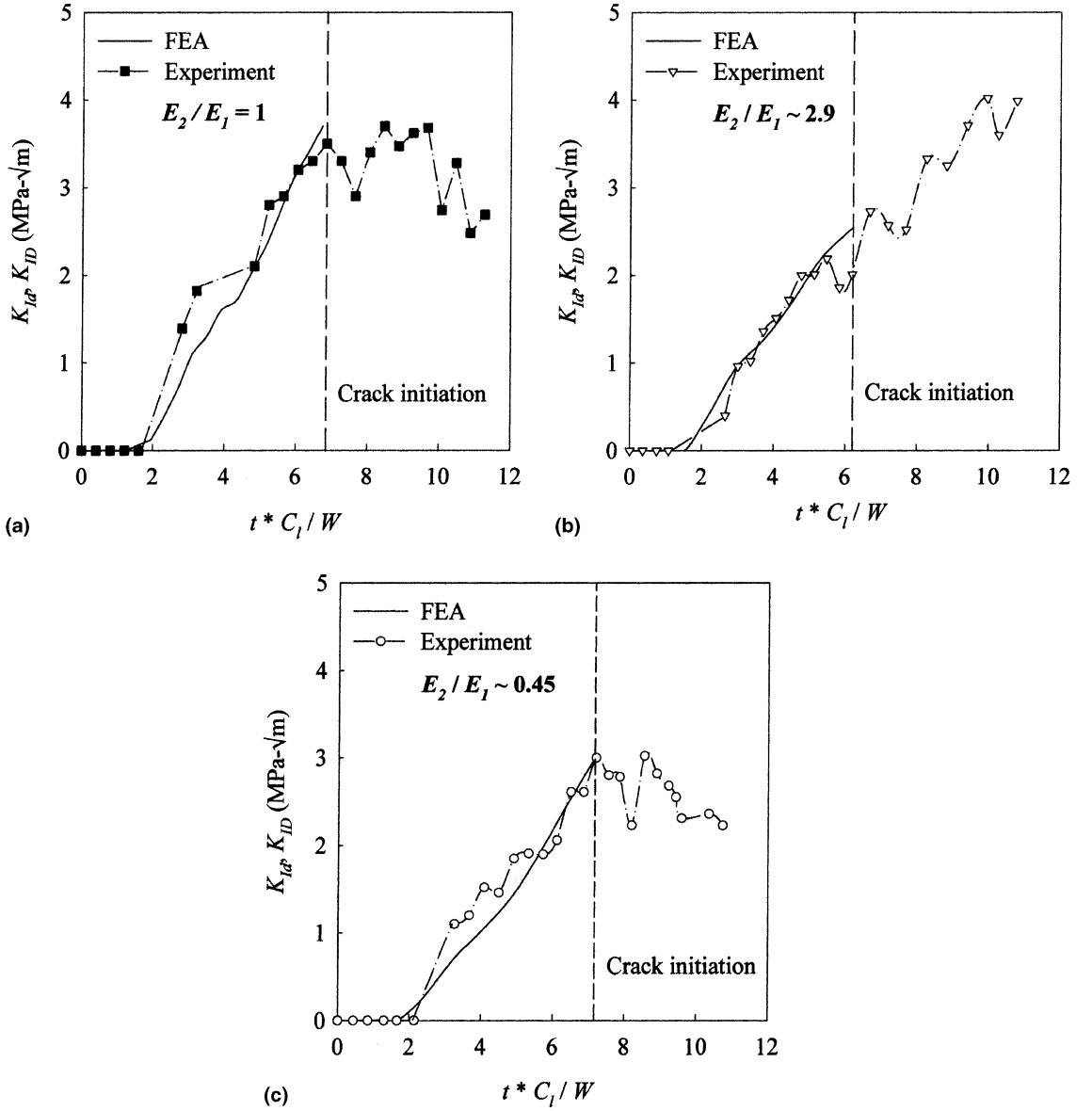

Fig. 9. Apparent mode-I dynamic stress intensity factor history for (a) homogeneous specimen; (b) FGM with crack on compliant side of gradient; (c) FGM with crack on stiff side of gradient.

mentally). Agreement between the two is remarkable. Note the absence of experimental data points for certain frames because of either loss of optical information and/or, during early stages of fringe formation, the fringes reside within the region of dominant triaxiality where they cannot be reliably analyzed. The homogeneous beam experiences a monotonic increase in $K_{ID}(t)$ until crack initiation. The dynamic initiation toughness is 3.3 ± 0.25 MPa $\sqrt{}$m. Following the initial crack extension, fluctuations are observed in the critical stress intensity factor, with a nearly constant value of K_{ID}. The average *apparent* toughness is about 3.3 MPa $\sqrt{}$m. Fluctuations in apparent toughness can be attributed to disturbances in the vicinity of the crack caused by the varying velocity.

The equivalent plot for the FGM with crack on the compliant side, $E_2/E_1 > 1$, is shown in Fig. 9(b). Again, excellent agreement exists between finite element and experimental results up to crack initiation occurring at $K_{ID} = 2.3 \pm 0.25$ MPa$\sqrt{}$m. Post crack initiation stress intensity factors in this case show an overall increasing trend with a superposed oscillatory behavior. The period of the oscillations approximately coincides with the time necessary for longitudinal waves to traverse back and forth once between the top and bottom edges of the specimen. The continuous rise in stress intensity factor with crack length can only be explained by increased toughness of the FGM at the successive crack tip locations, a very desirable attribute for a material. A maximum value of about 4 ± 0.25 MPa$\sqrt{}$m is attained in this sample. Indeed, crack propagation being driven by the critical value of the stress intensity, increased toughening requires continually increasing amount of energy for sustaining crack growth.

Experimental results for the *FGM with crack on the stiff side*, $E_2/E_1 < 1$, are plotted in Fig 9(c) along with those from numerical simulations. As before, there is good agreement between the two methods, prior to crack initiation. Based on the stress intensity factor history, crack initiation has occurred at a value of 3.0 ± 0.25 MPa$\sqrt{}$m. Again large post-initiation oscillations in stress intensity factor are present. A decreasing trend is also observed from the crack stress intensification history, which suggests decreasing fracture toughness with volume fraction.

At the moment, physical implications of $K_{ID}(t) - v$ (crack velocity) relationship for an FGM are unclear. Accordingly, crack growth resistance is plotted in Fig. 10 wherein $K_{ID}(t)$ values are normalized by the respective values at initiation. The figure illustrates the trend in each of the materials. An obvious upward slope is seen for the FGM with $E_2/E_1 > 1$, and a small but notable downward overall slope for $E_2/E_1 < 1$. Values for the homogeneous material are nearly constant over most of the crack growth region. Over the entire range of values, the results for the homogeneous material are generally bounded by the ones for FGMs. These observations are supported by inspection of the fractured surfaces. Micrographs corresponding to a location where $V_f \sim 0.4$ for the two FGMs are shown in Fig. 11. Again, for the FGM with $E_2/E_1 > 1$, the fractured surface shows substantially higher level of unevenness compared to the one for $E_2/E_1 < 1$. This appears to be at the root of higher values of *apparent* stress intensity factors that are measured optically.

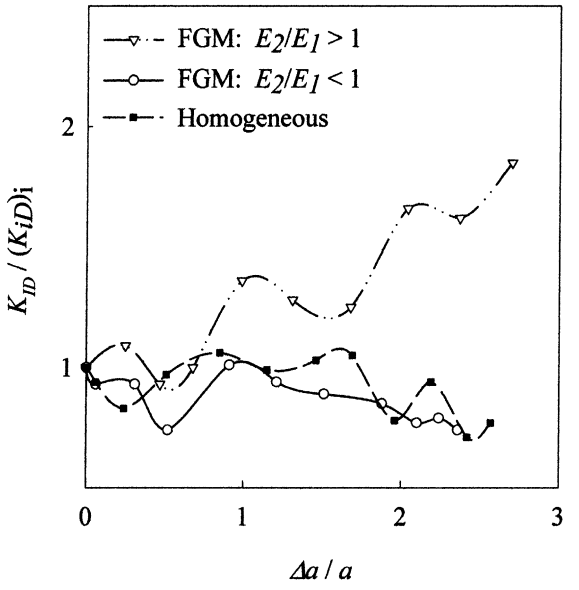

Fig. 10. Variation of apparent stress intensity factor with crack length.

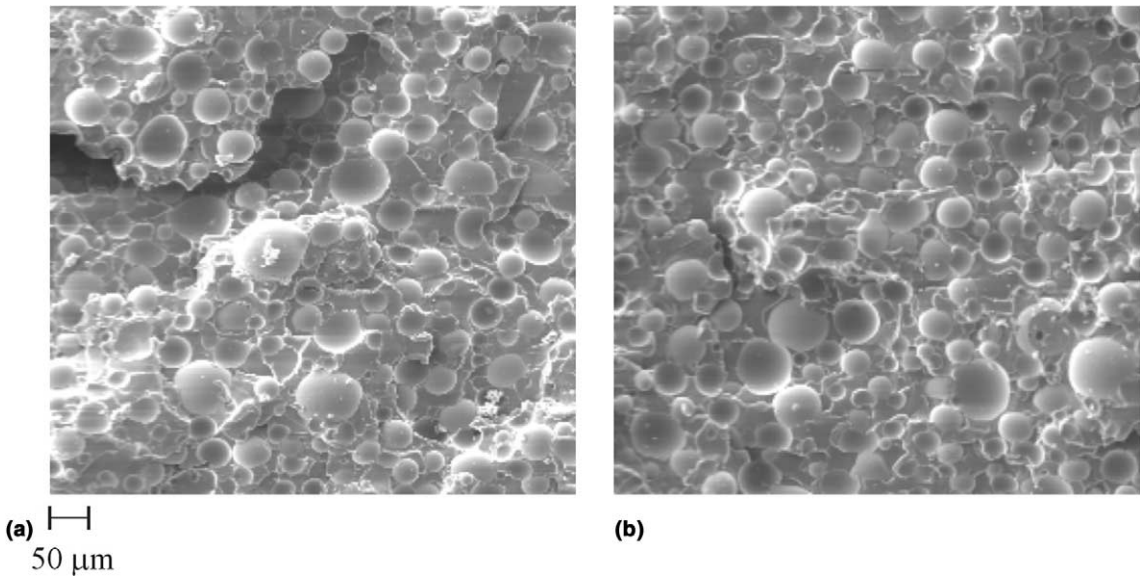

Fig. 11. Micrographs comparing FGM fractured surfaces ($V_f = 0.45$): (a) $E_2/E_1 > 1$; (b) $E_2/E_1 < 1$.

7.4. Dynamic fracture toughness

Differences in the pre-initiation stress intensity factor histories between FGMs and homogeneous samples can be directly attributed to their elastic characteristics. However, post-initiation data are affected by local fracture toughness characteristics as well. Here it is surmised that local fracture toughness is the dominant contributor to the observed behaviors (Fig. 9). This is confirmed by conducting dynamic toughness tests on several *homogeneous* samples with edge cracks, each having a constant volume fraction. Shallow notches were first cut into the beams, and were subsequently extended into sharp, natural cracks by applying a controlled force on a wedge inserted into the notch. The beams, 95 mm × 20 mm × 5.5 mm, were loaded in three-point bending by an Instron-Dynatup 8210 impact tester, at a speed of 1.5 m/s. This was achieved by releasing a 90 N (20 lb) deadweight along guide rails, from a designated height. Integral to the deadweight is a cylindrical tup, with a hemispherical end of radius 12.7 mm, that impacts the specimen directly opposite the crack. Affixed to the tup are sensors that feed information such as time, load and displacement history experienced by the tup to a computer. The maximum load registered at the tup was used to assess the dynamic crack initiation toughness. The information obtained through these tests is summarized in Fig. 12. (The rate of increase in stress intensity factor ($\dot{K}_{ID}$) prior to initiation in all specimens tested was ~20s MPa $\sqrt{}$m/ms and are different from the optical tests for which it was in the range of 38–54 MPa $\sqrt{}$m/ms but are used to demonstrate the trends.) The dynamic toughness

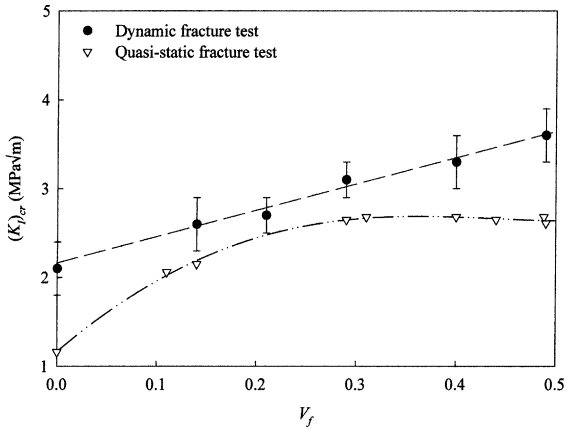

Fig. 12. Static and dynamic crack initiation toughness of glass-filled epoxy.

increases continuously with V_f, in addition to being consistently higher than quasi-static values. Dynamic initiation toughnesses vary from 2.1 to 3.6 MPa$\sqrt{m}$ as V_f increases from 0 to 0.49. These data points are close to those obtained from the optical analysis at similar volume fractions, suggesting that the FGM dynamic crack growth is indeed predominantly driven by local toughness values.

A related observation can be made here by contrasting the dynamic values (solid symbols) of apparent crack initiation toughness with the ones obtained quasi-statically (Rousseau and Tippur, 2000), shown by the broken line, in Fig. 12. Unlike the dynamic values which increase monotonically over the entire range of volume fraction of the filler, quasi-static values increase with volume fraction (from a value of $\sim$1.1 MPa$\sqrt{m}$) initially but level off beyond $V_f \sim 0.25$ (at a value of $\sim$2.7 MPa$\sqrt{m}$). An explanation to the upward shift in toughness from quasi-static to dynamic loading can be sought by examining the underlying material separation mechanism. In quasi-static situations, it was determined that as the glass spheres are added to the epoxy, the filler particles impede the motion of the crack by promoting interfacial separation and crack pinning mechanisms. At higher volume fractions, however, the presence of clusters of un-wet inclusions and pores increase and offset any improvement in fracture toughness. Similar behavior was expected also under dynamic conditions. However, the evidence suggests continual increase in fracture toughness with volume fraction.

Fig. 13 shows micrographs of two surfaces fractured, respectively, under quasi-static and dynamic conditions. Relatively smooth and leveled surface of the matrix interrupted by the particle footprints or the particles left behind in matrix in the quasi-static case are clearly evident. In contrast, added features of substantially rugged and uneven matrix in the dynamic case are clear. (It is important to point out that quasi-static and dynamic failures for all volume fractions always occur in the matrix. No evidence of broken glass spheres has been observed in these materials.) The ruggedness of the dynamic specimen surface caused by the microscale crack branching easily explains the higher levels of energy dissipation compared to static cases.

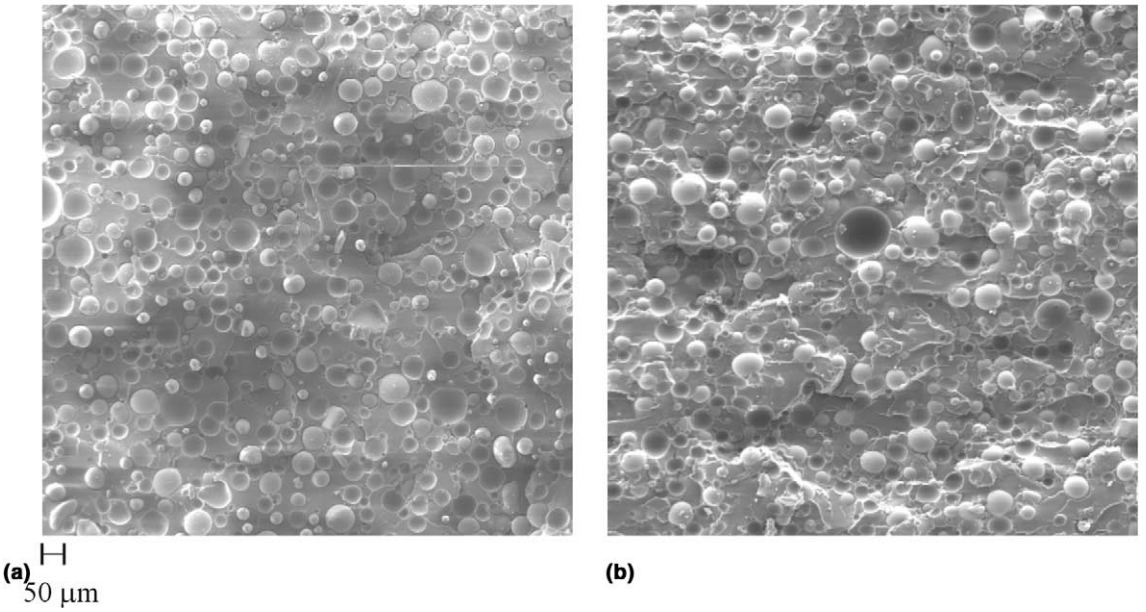

Fig. 13. Micrographs of (a) quasi-statically and (b) dynamically fractured FGM surfaces at a location where $V_f = 0.31$.

Another interesting surface feature is loosening of glass spheres from the matrix which is apparent in the quasi-static case. As the load increases at the crack tip, stress amplification appears to have separated matrix and particles which then act as voids that coalesce with the main crack. As the crack moves quasi-statically, energy in the near tip process zone is continuously transferred to adjacent areas, contributing to further debonding. To the contrary, dynamically broken surfaces show the glass beads to be well anchored and fully bonded to the epoxy. Glass beads are just circumvented by the crack during its approach, leaving the appearance of interfaces that are intact. Further, since the glass spheres are much stiffer than the matrix, the crack must meander its way between the glass beads, thus creating the rugged surface with microscopic branching seen in Fig. 13. It must be noted also that inertial effects typically increase the size of the process region at the crack tip and result in higher consumption of energy.

8. Conclusions

Crack tip deformations are studied in functionally graded materials having cracks parallel to the gradient direction and subjected to low-velocity, symmetric impact loading. The materials studied are compositionally graded glass-filled epoxy plates with monotonic unidirectional E/ρ variation of 4×10^6 to 6×10^6 $(\mathrm{m/s})^2$ along the height of the samples. The optical method of reflection CGS and high-speed photography were used to monitor surface slopes in the crack tip vicinity and in the far-field. Comparative studies between FGMs when cracks propagate from compliant side to the stiff side $(E_2/E_1 > 1)$ and vice versa $(E_2/E_1 < 1)$ were carried out. The results were also compared with samples made of homogeneous (constant volume fraction) glass/epoxy compositions. The deformation patterns at the impact location and in the far-field for the two FGM cases show significant differences when compared to the homogeneous composition due to continuously changing elastic characteristics. Under the idealization of macroscopically isotropic nonhomogeneous elastic material behavior, interferograms have been analyzed. Quasi-static expressions for the FGM deformation fields were used to analyze interferograms prior to crack initiation, whereas recently developed equations for FGMs with steadily growing cracks were used to evaluate post-initiation fringes. The use of crack tip fields based on locally homogeneous material assumption for a steadily growing dynamic crack in FGMs was found to provide K_{ID} results that are within a few percent from the ones that incorporate material nonhomogeneity for the specific material studied. Finite element simulations of the same up to crack initiation were also undertaken and good agreement with the experimental results were observed. The crack initiation in homogeneous materials is seen to occur at times between that for the two FGMs, with the FGM with crack on the compliant side experiencing it earlier. This is due, in the latter case, to the acceleration of the stress waves as they reflect from the bottom edge of the beam, whereas these remain at a constant speed for the homogeneous beam, and decelerate for the other FGM. Features of the crack growth included a sharp rise in velocity followed by a decrease of equal rate, with the FGM having a crack on the compliant side attaining its peak with a delay when compared to the other specimens. The FGM having the crack on the stiff edge exhibits higher crack deceleration. Post-initiation apparent stress intensity factors increase continuously with time as the crack propagates towards the stiffer side of the FGM. On the other hand, a decreasing trend is observed when the crack advances towards the more compliant side from the stiff side of an FGM. In the homogeneous sample, however, the dynamic SIF for the growing crack remains nearly constant during the same period. The crack growth resistance curves for these samples confirm these observations, showing the homogeneous sample sandwiched between the two FGMs. The optical measurements are complemented by fracture surface morphology studies. Increased V_{f} of the filler is shown to be at the source of the continuously increasing fracture toughness seen in the FGM for which crack growth occurs in the direction of increasing volume fraction.

Acknowledgements

The support of this research by ARO Solid Mechanics Program (DAAG55-97-1-0110 and DAA D19-01-1-0414) is gratefully acknowledged.

References

Babaei, R., Lukasiewicz, S.A., 1998. Dynamic response of a crack in a functionally graded material between two dissimilar half-planes under anti-plane shear impact load. Engineering Fracture Mechanics. 60 (4), 479–487.

Butcher, R.J., Rousseau, C.-E., Tippur, H.V., 1999. A functionally graded particulate composite: preparation, measurements and failure analysis. Acta Materialia 47 (1), 259–268.

Chiu, T.C., Erdogan, F., 1999. one-dimensional wave propagation in a functionally graded elastic medium. Journal of Sound and Vibration. 222 (3), 453–487.

Delale, F., Erdogan, F., 1983. The crack problem for a nonhomogeneous plane. ASME Journal of Applied Mechanics. 50, 609–614.

Eischen, J.W., 1987. Fracture of nonhomogeneous materials. International Journal of Fracture 34, 3–22.

Freund, L.B., Clifton, R.J., 1974. On the uniqueness of plane elastodynamic solutions for running cracks. Journal of Elasticity 4 (4), 293–299.

Jin, Z.-H., Noda, N., 1994. Crack-tip singular fields in nonhomogeneous materials. ASME Journal of Applied Mechanics 61, 738–740.

Johnson, K.L., 1998. Contact Mechanics. Cambridge University Press, Cambridge.

Marur, P.R., Tippur, H.V., 2000a. Dynamic response of bimaterial and graded interface cracks under impact loading. International Journal of Fracture 103, 95–109.

Marur, P.R., Tippur, H.V., 2000b. Numerical analysis of crack-tip fields in functionally graded materials with a crack normal to the elastic gradient. International Journal of Solids and Structures 37, 5353–5370.

Nakagaki, M., Wu, Y.D., Hagihara, S., 1998. Dynamically propagating crack in graded particle dispersed composites. Fracture and Strength of Solids 145, 333–342.

Parameswaran, V., Shukla, A., 1998. Dynamic fracture of a functionally gradient material having discrete property variation. Journal of Materials Science 33, 3303–3311.

Parameswaran, V., Shukla, A., 1999. Crack-tip stress fields for dynamic fracture in functionally gradient materials. Mechanics of Materials 31, 579–596.

Parameswaran, V., Shukla, A., 2000. Private communications.

Rousseau, C.-E., 2000. Evaluation of crack tip fields and fracture parameters in functionally graded materials. Ph.D. Dissertation, Auburn University.

Rousseau, C.-E., Tippur, H.V., 2000. Evaluation of crack tip fields and stress intensity factors in functionally graded elastic materials: crack parallel to elastic gradient (submitted).

Tippur, H.V., Krishnaswamy, S., Rosakis, A.J., 1991. A coherent gradient sensor for crack tip deformation measurements: analysis and experimental results. International Journal of Fracture 48, 193–204.